ACS NANO

www.acsnano.org

ARTICLE

Ultrafast Dual-Shock Chemistry Synthesis of Ordered/Disordered Hybrid Carbon Anodes: High-Rate Performance of Li-Ion Batteries

Pengfei Huang, Zekun Li, Li Chen, Yuan Li, Zhedong Liu, Jingchao Zhang, Jiawei Luo, Wenjun Zhang, Wei-Di Liu, Xinxi Zhang,* Rongtao Zhu,* and Yanan Chen*

Cite This: *ACS Nano* 2024, 18, 18344−18354

Read Online

ACCESS | Metrics & More | Article Recommendations | Supporting Information

ABSTRACT: Graphite exhibits crystal anisotropy, which impedes the mass transfer of ion intercalation and extraction processes in Li-ion batteries. Herein, a dual-shock chemical strategy has been developed to synthesize the carbon anode. This approach comprised two key phases: (1) a thermal shock utilizing ultrahigh temperature (3228 K) can thermodynamically facilitate graphitization; (2) a mechanical shock (21.64 MPa) disrupting the $\pi-\pi$ interactions in the aromatic chains of carbon can result in hybrid-structured carbon composed of crystalline and amorphous carbon. The optimized carbon (DSC-200−0.3) demonstrates a capacity of 208.61 mAh/g at a 10C rate, with a significant enhancement comparing with 15 mAh/g of the original graphite. Impressively, it maintains 81.06% capacity even after 3000 charge−discharge cycles. Dynamic process analysis reveals that this superior rate performance is attributed to a larger interlayer spacing facilitating ion transport comparing with the original graphite, disordered amorphous carbon for additional lithium storage sites, and crystallized carbon for enhanced charge transfer. The dual-shock chemical approach offers a cost-effective and efficient method to rapidly produce hybrid-structured carbon anodes, enabling 10C fast charging capabilities in lithium-ion batteries.

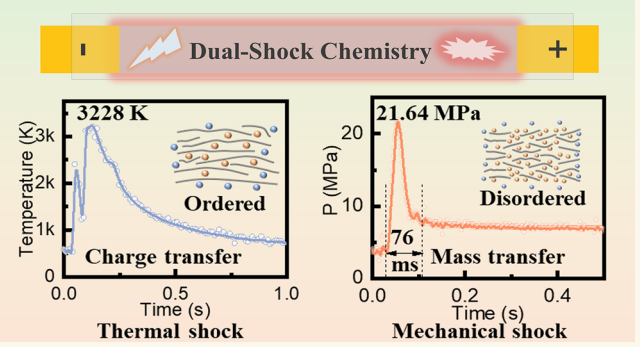

KEYWORDS: *dual-shock chemistry, ordered/disordered hybrid carbon, ultrafast synthesis, high-rate performance, Li-ion batteries*

INTRODUCTION

The increasing requirement to reduce the charging times of electric vehicles has propelled fast-charging, high-energy-density lithium-ion batteries to the forefront of practical applications.[1] However, the current charging duration for most electric vehicles, typically ranging from 2 to 6 h, which failed to provide a user experience akin to refueling a traditional vehicle (3−6 min).[2] This discrepancy hampers the widespread adoption of electric vehicles.[3] The fundamental limit stems from the crystal anisotropy of graphite, commonly used as an anode material in lithium-ion batteries.[4] This anisotropy restricts the movement of lithium ions within the graphite, particularly impeding the mass transfer of ion intercalation and extraction processes.[5] More specifically, the sluggish migration of lithium ions at the graphite sheet interface is a critical bottleneck in achieving high current performance.[6] Therefore, addressing this challenge necessitates the development of power batteries capable of charging at rates exceeding 10C, which can further enable a complete charge in under 6 min.[3]

To tackle the issue of low mass transfer rates in graphite anodes, researchers have implemented various strategies to enhance Li^+ mass transfer efficiency.[7] Among them, the creation of nanoscale pores in the graphite structure via etching and expansion[8,9] methods to increase the spacing between graphitic carbon layers are typical efficient strategies. Additionally, doping on the carbon layer surface with sulfur and nitrogen can boost the adsorption capacity for Li^+,[10] thereby improving transport efficiency.[11] However, the core limit of graphite in fast-charging applications is the slow diffusion kinetics of lithium ions in the graphite interlayers[12] and sluggish interfacial reaction kinetics.[13] To address these

Received: February 18, 2024
Revised: June 25, 2024
Accepted: June 27, 2024
Published: July 2, 2024

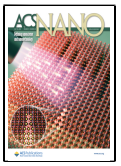

https://doi.org/10.1021/acsnano.4c02300
ACS Nano 2024, 18, 18344−18354

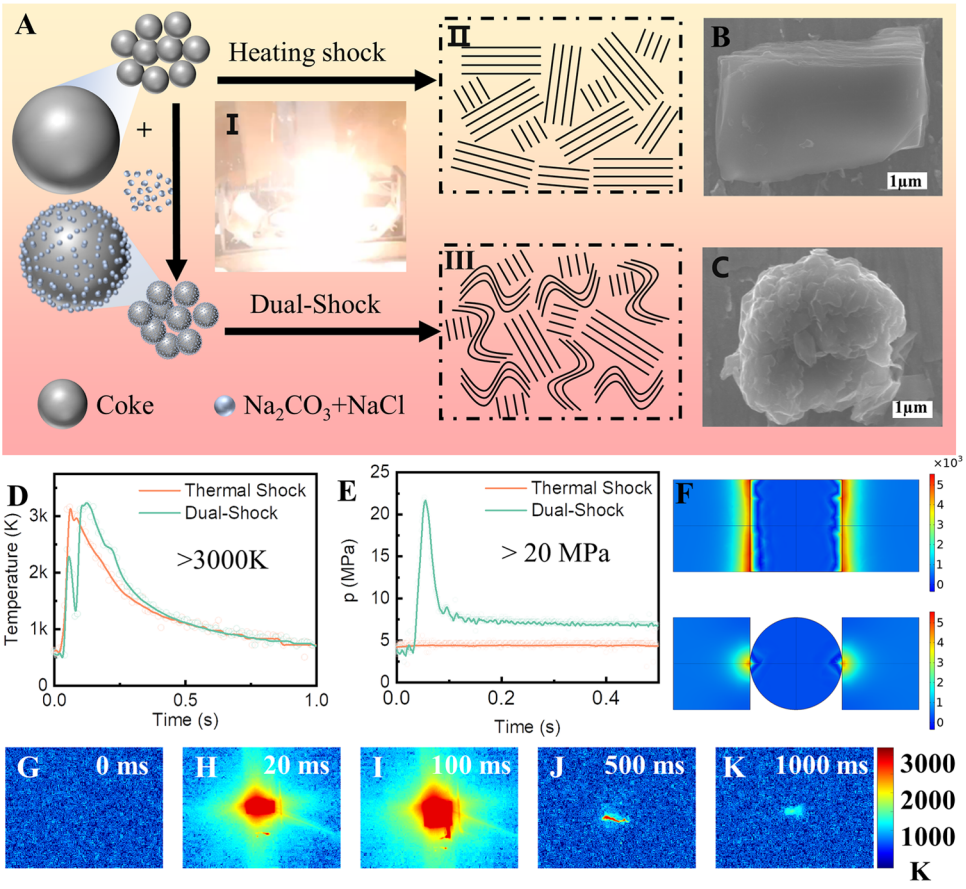

Figure 1. (A) Schematic comparison between the thermal-shock and dual-shock chemical strategy. (B) SEM images of samples treated with thermal shock and (C) dual-shock process. (D) The temperature−time evolution over approximately 1 s after dual-shock and thermal-shock treatment processes. (E) The press-time evolution during the approximately 0.5 s. (F) COMSOL simulation of temperature distribution for various contact modes. (G−K) Temperature distribution throughout the dual-shock process at different time intervals.

challenges, anode materials, such as hybrid-structured carbon anodes composed of both graphite and hard carbon, have been developed.[12] These hybrid-structured carbon anodes enhance reaction current uniformity and overall performance. Moreover, researchers have also innovated an ion-pumped interphase (IPI) structure anode.[14] This anode enhances mass and charge transfer efficiencies by forming a graphene (GDY)/graphite heterojunction at the graphite surface. Nevertheless, the complexity and high energy consumption of these processes pose significant industrial application challenges.[15] Consequently, there is a pressing need for a simpler, more controllable, and more efficient preparation method that can cater to the production requirements of carbon anodes with enhanced mass and charge transfer efficiencies.[16]

In response to the demand for more efficient graphitization methods, thermal shock[17] emerges as a promising alternative that can offer significant time and energy savings compared to traditional techniques. However, applying direct high-temperature thermal shock to carbon precursors typically results in the formation of highly ordered graphite-like structures.[18] To address this challenge, we have developed an in situ dual-shock chemistry strategy for the ultrafast synthesis of hybrid-structured carbon anodes. This strategy employs sodium carbonate (Na_2CO_3) and sodium chloride (NaCl) as activators to facilitate mechanical shock via gas generation. The ultrahigh energy discharged from a 100 mF capacitor creates high-density microexplosion sites, enabling ultrahigh temperature thermal shock. This approach has led to the creation of the optimized thermal shock synthesis carbon and the dual-shock chemistry process synthesis carbon. It is demonstrated that lithium-ion batteries using these anodes maintain 81.06% specific energy retention after 3000 cycles at a 10C fast charge rate, which is a significant improvement over the 54.44% retention rate of the thermal shock carbon under identical conditions. Notably, dual-shock chemistry process synthesis carbon exhibits exceptional electrochemical performance, delivering 208.61 mAh/g (comparing to the 15 mAh/g of commercial graphite). The exceptional rate performance can be attributed to the expanded interlayer spacing, which facilitates mass transport.[19] Furthermore, a hybrid-structured carbon is incorporated, where disordered amorphous carbon can provide additional lithium storage sites, and structured graphite crystallites can enhance charge transfer.[20] The battery performance achieved in this study aligns with the Department of Energy's objectives for fast-charging, high-energy-density lithium-ion batteries.[3]

RESULTS AND DISCUSSION

Dual-Shock Chemistry. Figure S1 illustrates the synthesis of dual-shock chemistry using a homemade device. In this process, a customized capacitor array (60 mF) is employed to apply varying voltages. This application generates Joule heating, allowing precise control of temperature and duration.

https://doi.org/10.1021/acsnano.4c02300
ACS Nano 2024, 18, 18344−18354

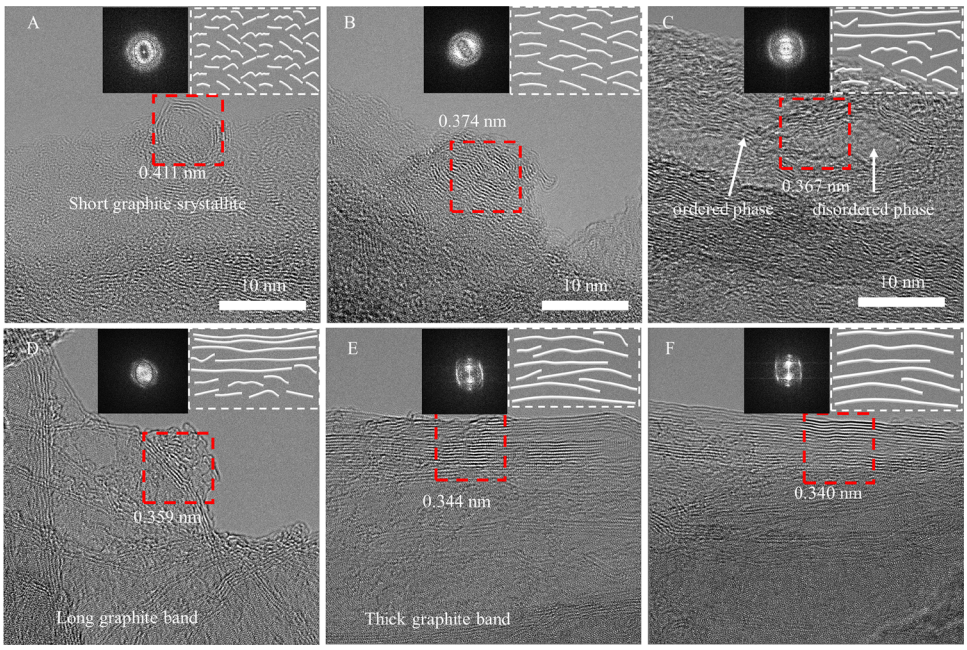

Figure 2. High-resolution transmission electron microscopy (HRTEM) images of (A) DSC-150−0.3, (B) DSC-175−0.3, (C) DSC-200−0.3, (D) DSC-225−0.3, (E) DSC-250−0.3, and (F) TSC-200, along with their corresponding fast Fourier transform (FFT) pattern in the red rectangular area, are presented.

In the case of DSC-200−0.3 (DSC: Dual-shock carbon), a mass ratio of 3:7 between the activator and petroleum coke is achieved through mechanical stamping, creating a uniform mixture. This mixture consists of 70 mg of petroleum coke and 30 mg of activator (Na_2CO_3 and NaCl in a 1:1 ratio, with "0.3" indicating the activator ratio in the precursor). Subsequently, this blend undergoes high-temperature reaction synthesis in the customized device at 200 V, generating the previously mentioned bright white light, accompanied by substantial heat and pressure (as depicted in Figure 1A-I). Rinse the sample with hydrochloric acid and deionized water until neutral to mitigate the influence of sodium (Na) and chlorine (Cl) elements originating from Na_2CO_3 and NaCl in the precursor on the electrochemical performance. In samples without an activator (TSC-200, comprising only 100 mg of petroleum coke and subjected to 200 V to induce thermal shock), the surface of the sample particles exhibits a smooth and uniform appearance (as shown in Figure 1B). This structure arises from the orderly stacking of graphite layers in carbon materials subjected to extreme thermal shock (as illustrated in Figure 1A-II). In contrast, the introduction of an activator, along with thermal and mechanical shocks, yields distinct surface properties in the sample particles. This is featured by a rough surface with numerous pits and irregular pores (as depicted in Figure 1C). The formation of these pores is primarily a result of the high-temperature decomposition of Na_2CO_3 in the activator, which generates CO_2 gas and Na vapor.[21] Furthermore, in the synthesis process of dual-shock chemistry, the ultrahigh temperature can thermodynamically induce the graphitization of carbon, while the mechanical shock simultaneously causes the bending of the graphite layer (as illustrated in Figure 1A-III). These two factors collaborate to form a distinctive hybrid-structured, incorporating ordered graphite and disordered amorphous carbon in the material.

To analyze the temperature and pressure changes during the dual-shock chemistry process from both kinetic and thermodynamic perspectives, a homemade measuring device (depicted in Figure S2) was employed to conduct precise measurements. As illustrated in Figure 1D, the rate of temperature increase reaches 10^5 K/s due to Joule heating, while the cooling rate is 10^4 K/s. The peak temperature surpasses 3000 K, enabling the reaction to complete within a millisecond. In the dual-shock chemistry process, with the introduction of the activator, the temperature−time profile reveals significant fluctuations during the heating phase. These fluctuations are attributed to the gas shock wave generated by the high-temperature decomposition of the activators, momentarily disrupting the connectivity within the samples. Simultaneously, the thermal decomposition of the activator rapidly enlarges the sample's internal volume, resulting in a significant increase in internal pressure (as illustrated in Figure 1E). The internal pressure, measured by the pressure sensor, exceeded 20 MPa for a duration of 76 ms. Notably, samples exposed solely to thermal shock exhibited minimal pressure variation. In summary, this ultrahigh temperature thermal shock ensures the synthesis of graphite microcrystals from the thermodynamic perspective. Simultaneously, it dynamically disrupts the crystal structure under high-pressure mechanical shock and promotes a disordered arrangement. This dual-shock chemistry strategy provides a method for the thermodynamic and kinetic synthesis of hybrid-structured carbon.

To gain deeper insights into the temperature distribution within particles during Joule heating reactions, we employ the COMSOL model to explore three distinct contact modes within various particles: surface contact, line contact, and point contact (as illustrated in Figure S3). The simulation results unveiled a significant temperature variation specifically at the contact points. Interestingly, when comparing samples composed of a single substance to heterogeneous systems, the former exhibited a less pronounced temperature change at the contact surface. This distinction arises from the

https://doi.org/10.1021/acsnano.4c02300
ACS Nano 2024, 18, 18344−18354

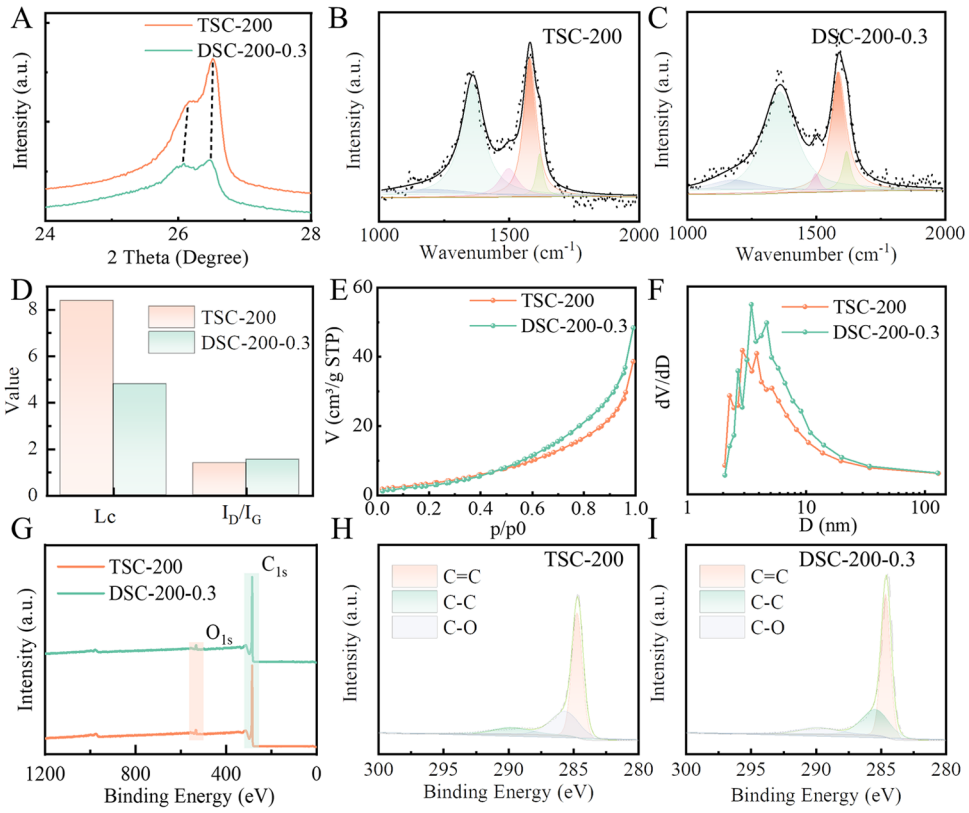

Figure 3. Structural evolution of the dual-shock process: (A) XRD patterns of DSC at different voltages. Raman patterns of (B) TSC-200, (C) DSC-150−0.3; (D) lattice length and I_D/I_G values of DSC and TSC. (E) N_2 adsorption/desorption isotherms and (F) pore size distribution curves of the TSC-200 and DSC-200−0.3; (G−I) The XPS pattern of TSC-200 and DSC-200−0.3.

inhomogeneous material composition within the particles and varying particle sizes, resulting in uneven current distribution and, consequently, diverse heat generation. At the contact points between particles, there is a notable fluctuation in current density, where regions with high current density generate more heat. Consequently, contact points experience more fluctuating local temperatures (Figure 1F). As a result, incorporating an activator amplifies the intensity of reactions at the carbon contact surface during the dual-shock chemistry process.

During the analysis of temperature and heating rate in dual-shock chemistry strategy synthesis, we utilized high-speed camera images as a valuable tool (see Figure S4). These images effectively capture the diffusion of white light throughout the sample within 20 ms, reaching a maximum after 100 ms, with an expansion in volume. By correlating blackbody radiation with temperature, we generated a temperature distribution cloud diagram (Figure 1G−K), indicating a uniform temperature distribution throughout the reaction. This consistency aligns with the temporal temperature changes depicted in Figure 1D during dual-shock chemistry synthesis.

In summary, the utilization of the dual-shock chemistry strategy, triggered by activators, facilitated the rapid rise and fall of temperatures, accompanied by internal pressure changes. These factors played a crucial role in advancing the thermodynamic synthesis of graphite microcrystals and inducing the disruption of the crystal structure under high-pressure mechanical shock, ultimately leading to the formation of a hybrid-structured carbon. In contrast to traditional tube furnaces, acknowledged for their time-intensive and inefficient characteristics, the dual-shock chemical strategy stands out as notably advantageous in terms of high efficiency and swift preparation.

Structural Evolution of the Dual-Shock Process. Figure 2A−E presents high-resolution transmission electron microscopy (HRTEM) images of samples synthesized using the dual-shock chemical strategy. At low voltages (DSC-150−0.3 and DSC-175−0.3), the predominant morphological features are short graphite crystallites, with their fast Fourier transform (FFT) patterns as polycrystalline rings, indicative of a primarily amorphous carbon composition. As the voltage increases to DSC-200−0.3, these short graphite crystallites begin merging into curved graphite ribbons. And a portion of the amorphous carbon integrates, forming a hybrid structure. Simultaneously, the amorphous regions diminish, signifying an increase in structural ordering. Figure S6 represents the measurement of interplanar spacing, revealing a gradual decrease with increasing voltage, indicating a rising degree of graphitization. In comparison, graphite layers in DSC-200−0.3, subjected to the dual-shock chemistry strategy, appear more disordered with wider interlayer spacing compared to those in samples solely subjected to thermal shock (TSC-200) (Figure 2F). Upon further elevation of the voltage to DSC-225−0.3 and DSC-250−0.3 (as shown in Figure 2D,E), the ordered structure within the samples becomes more pronounced, evolving into extended graphite bands. This transformation is accompanied by a noticeable thickening of the graphite layers, resembling the structure of commercial graphite (Figure S7). All of these observations indicate that the dual-shock chemical strategy effectively moderates the $\pi-\pi$ interactions among aromatic chains in the carbon material. This moderation impedes the ordering of microcrystals, resulting in a hybrid

https://doi.org/10.1021/acsnano.4c02300
ACS Nano 2024, 18, 18344−18354

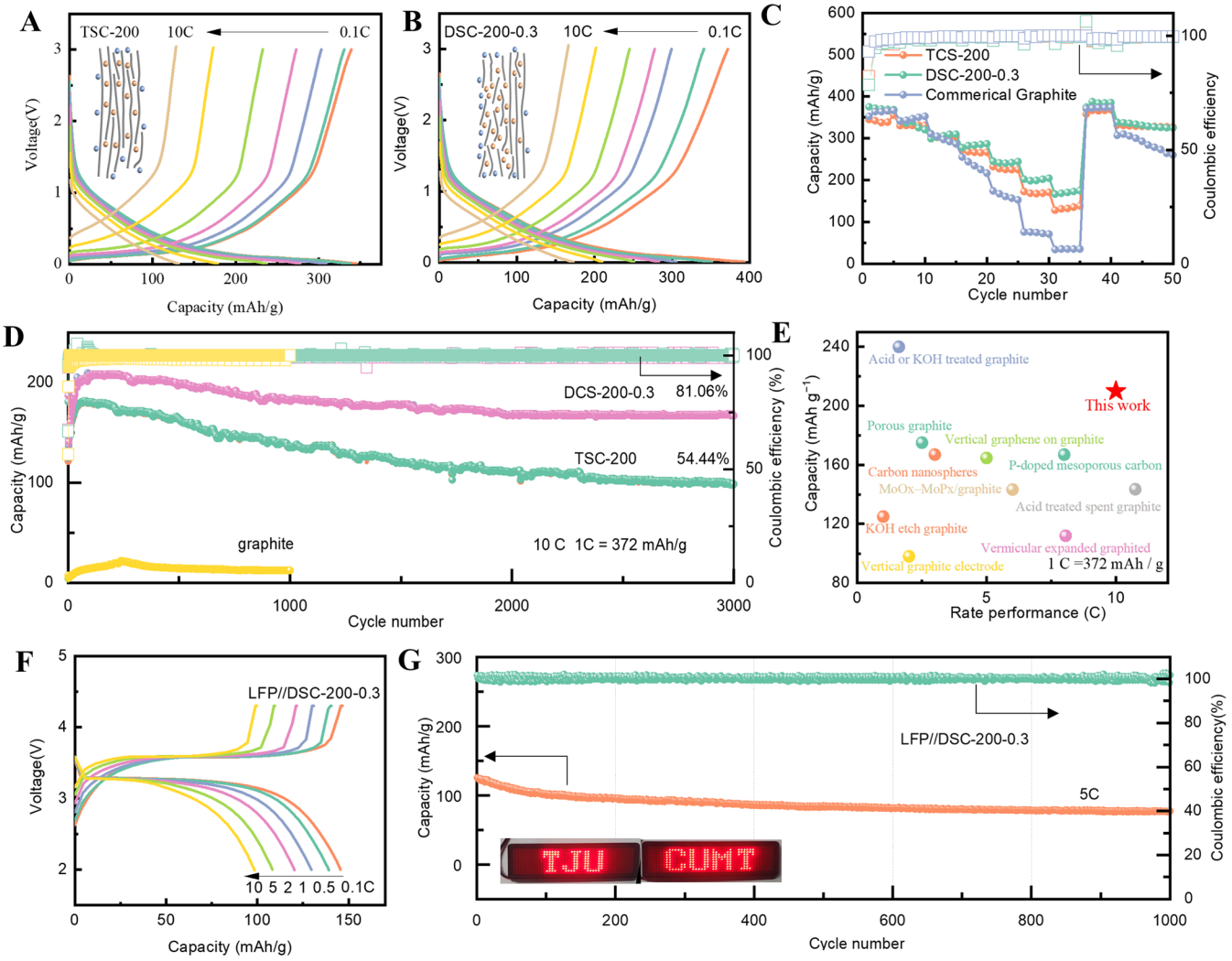

Figure 4. Electrochemical performance of the TSC-200 and DSC-200 as LIBs anodes in half cells: (A) Charge/discharge curves and at different current densities of TSC-200 and (B) DSC-200−0.3. (C) Rate capability. (D) Cycling performance at 10C. (E) Comparison of the capacity and rate performance between this work and reported literatures. (F) Full cell LFP||DSC-200−0.3 rate capability and (G) cycling performance at 5C.

structure that encompasses both disordered and ordered phases.

Quantitative analysis of the structural modifications and crystallinity in the samples was conducted via X-ray diffraction (XRD). Figures S8−S10A reveals an asymmetric peak within the 24−28°[22] range. In Figure S8, an elevation in discharge voltage results in the narrowing and moves to a higher angle of the graphite 002 peak, implying enhanced graphite crystallinity and reduced interlayer spacing. The (002) diffraction peak of DSC obviously moves to a lower angle and becomes wider[23] in Figure S9. However, introducing an activator into the DSC samples under identical voltage conditions led to more slow changes in the 002 peak, as shown in Figure S10. This observation suggests that the activator potentially restricts the orderly stacked graphite layers, aligning well with HRTEM findings. Moreover, adjusting the activator's proportion (as shown in Figure S10) allows manipulating the content of ordered and amorphous phases. Further analysis involved utilizing the Scherrer formula[23] to calculate the crystallite size, labeled as L_c, detailed in Figures S8−S10. It is noted that above 200 V (Figure S9), a considerable elongation of the graphite lattice and an increased proportion of ordered carbon are observed simultaneously. Figure 3A compares the XRD patterns of samples (TSC-200 and DSC-200−0.3) under identical conditions. The sharper 002 peak in thermal-shock carbon suggests that the addition of an activator hinders the growth of graphite crystallites.

The Raman spectra further corroborated the findings from the XRD analysis. When comparing the Raman spectra of TSC (Figure S11) and DSC (Figure S12) samples under diverse conditions, it is evident that all samples exhibit two distinct peaks in the D and G bands, located approximately at 1350 and 1585 cm^{-1}, respectively. The D band typically signifies disordered and defective carbon, while the G band is associated with the in-plane vibrational motion of sp^2-bonded carbon atoms reflecting graphitic carbon characteristics.[4] Additionally, the intensity ratio of these peaks (I_D/I_G) serves as an indicator of defects, disorder, and the degree of graphitization in carbon materials. A narrower G band and lower I_D/I_G values of the TSC samples (Figure S11) suggest a higher degree of graphitization and a more ordered, flawless graphite structure. Conversely, the I_D/I_G ratio in DSC samples (Figure S12) escalates markedly post dual-shock treatment, signifying a reduction in graphitization. Furthermore, varying

https://doi.org/10.1021/acsnano.4c02300
ACS Nano 2024, 18, 18344−18354

activator ratios (Figure S13) demonstrate a decline in I_D/I_G values, implying that the activator can impede the graphitization process. These observations align with the XRD analysis results. Figure 3B compares the Raman patterns of samples (TSC-200 and DSC-200−0.3) under identical conditions. The smaller D peak and larger crystallite size in thermally shocked carbon suggest fewer defects and a higher degree of graphitization, as shown in Figure 3D.

The application of the dual-shock chemical strategy not only changes the structural composition but also significantly affects the morphology of carbon. This transformation is clearly illustrated in the scanning electron microscopy (SEM) images presented in Figure S14. As the amount of activator increases, noticeable alterations in the material morphology are observed. Initially, carbon exhibits a flat sheet-like structure with a smooth and regular surface. However, with the gradual introduction of the activator, the structure of the carbon changes from flat plates into rod-like structures. The appearance of these rod-like structures indicates that the mechanical force exerted by the activator can lead to the reconstruction and fragmentation of carbon. This transformation leads to a reduction in particle size, which is beneficial to reducing the diffusion path of lithium ions, thereby enhancing its dynamic condition and improving the rate performance. The type III adsorption−desorption isotherm,[24] depicted in Figure 3E, reveals that both TSC-200 and DSC-200−0.3 exhibit low specific surface areas, measuring 9.7 and 11.7 m^2/g, respectively. Simultaneously, the pore size distribution in Figure 3F indicates only a slight increase in pore diameter, with the most probable pore diameter being 3.45 and 3.86 nm for TSC-200 and DSC-200−0.3, respectively. These findings collectively suggest that the dual-shock chemical process predominantly shocks the surface pore structure of the sample, with the interior displaying relatively low porosity. This observation holds significant implications for reducing the first Coulombic efficiency.

For a more in-depth exploration of the chemical changes during the reaction, X-ray photoelectron spectroscopy (XPS) was employed. The XPS characterization results of TSC-200 and DSC-200−0.3 are illustrated in Figure 3G. The full spectrum reveals minimal oxygen peaks in the sample, suggesting an enhancement in the elemental purity of carbon through the dual-shock chemical process. Upon comparing the high-resolution C 1s spectra of the two samples, the C═C bond ratio in the DSC-200−0.3 sample (Figure 3I) is found reduced in contrast to TSC-200 (Figure 3H), further demonstrating the inhibition of the graphitization process. These findings highlight that, by finely adjusting activator ratios and voltages, precise control over the content between ordered and disordered carbon can be achieved, allowing manipulation of the material morphological dimensions.

High-Rate Performance of Li-Ion Batteries. The electrochemical performance of TSC and DSC electrodes was investigated in Li/Carbon half-cells to compare their rapid charging capabilities as anode materials for lithium-ion batteries (LIBs). Analysis of the galvanostatic charge−discharge curves of DSC and TSC electrodes, conducted at a current density of 0.1C (illustrated in Figure S15), revealed that DSC-200−0.3 and TSC-200 exhibited the highest reversible specific capacities. Consequently, these samples were selected for subsequent comparative electrochemical testing. Figure 4A−C provides a detailed comparison of the electrochemical behaviors of DSC-200−0.3 and TSC-200 electrodes, showing their rate performance across seven current rates ranging from 0.1 to 10C over five cycles, along with their charge/discharge curves. Specifically, at the low current rate of 0.1C, the initial charging capacity of the DSC-200−0.3 electrode was 375.6 mAh/g, as depicted in Figure 4B. As the current rate incrementally increases, the electrode demonstrates average charging capacities of 351.1, 299.4, 277.6, 245.3, 202.2, and 166.6 mAh/g at current densities of 0.2, 0.5, 1, 2, 5, and 10C, respectively. It is important to note that these rate performance values are likely underestimates, as the carbon material requires a longer activation period. Moreover, after undergoing secondary charge−discharge cycles at various current densities and then reverting suddenly to 1 and 0.1C, the charging capacity of the DSC-200−0.3 electrode recovered to 371.1 and 338.8 mAh/g, respectively (Figure 4C). This recovery indicates that the DSC-200−0.3 electrode possesses superior rate capability and enhanced reversibility, particularly at a current rate of 0.1C. In contrast, the TSC sample initially exhibits a charge capacity of 344.1 mAh/g at 0.1C, while the commercial graphite sample reaches 352.6 mAh/g.

Figure 4D illustrates the cycling stability and Coulombic efficiency of DSC-200−0.3 and TSC-200 electrodes over 3000 cycles at a current rate of 10 C. Initially, the HTC electrode displays a capacity of 208.6 mAh/g, maintaining 169.1 mAh/g after 3000 cycles. This corresponds to a capacity retention of approximately 81.06%. Meanwhile, the THC exhibits a peak capacity of only 181.85 mAh/g, with a similar capacity retention rate of about 81.06% after 3000 cycles. These outcomes demonstrate that the DSC-200−0.3 sample has exceptional cycling performance and electrochemical stability as an anode material for lithium-ion batteries (LIBs). Electrochemical impedance spectroscopy (EIS) spectra of TSC-200 and DSC-200−0.3 after 3000 cycles are presented in Figure S16. The measured charge transfer resistances (R_{ct}) are 60.2 Ω for TSC-200. In contrast, the DSC-200−0.3 only demonstrates the R_{ct} of 35.1 Ω, with almost no increase compared to the initial state. This comparison evidences the enhanced charge transfer kinetics of the DSC-200−0.3. Additionally, Figure 4E compares the high-rate charge capacities of the carbon materials developed in this study with various other carbon materials reported in the literature, including graphite synthesized by other methods,[7,25−32] where the DSC-200−0.3 demonstrates outstanding performance. To assess the practical viability of DSC-200−0.3 in real-world applications, full cells were assembled by coupling it with a LiFePO4 (LFP) cathode. As depicted in Figure 4F, the full cell LFP//DSC-200−0.3 consistently exhibits superior rate performance with increasing charging rates. Additionally, a cycling test reveals that the full cell LFP||DSC-200−0.3 exhibits outstanding capacity retention, reaching 61.12% after 1000 cycles at 5C, while maintaining a stable Coulombic efficiency close to 100% (Figure 4G). These results underscore the feasibility of DSC-200−0.3 in fast-rechargeable, high-energy battery applications. These findings suggest that the hybrid-structured carbon anodes offer more advantageous rate performance and reversible capacity, solidifying their potential as an effective anode material for LIBs.

Dynamic Process Analysis. To delve deeper into the reasons behind the rate performance of the hybrid carbon anodes, kinetic analyses were conducted on TSH-200 and DSC-200−0.3 electrodes. Galvanostatic Intermittent Titration Technique (GITT) results (displayed in Figure 5A,B) reveal

https://doi.org/10.1021/acsnano.4c02300
ACS Nano 2024, 18, 18344−18354

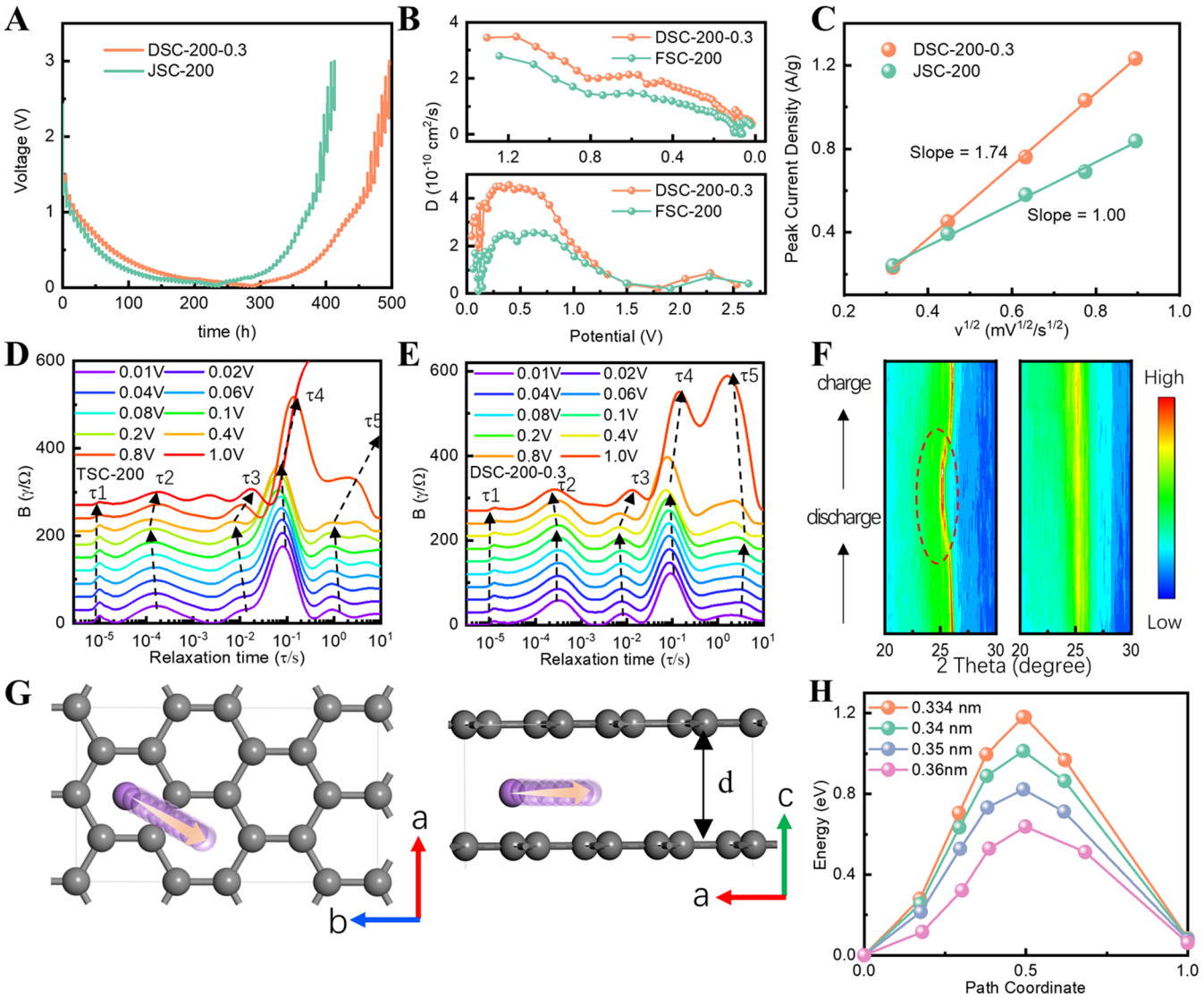

Figure 5. Kinetic analysis of the electrochemical behavior for TSC-200 and DSC-200−0.3 electrodes: (A) GITT profiles of GITT profiles of TSC-200 and DSC-200−0.3 anode; (B) Li ion diffusion coefficients at sodiation process (top-plot) and desodiation process (bottom-plot) estimated from GITT curves. (C) Relationship between the square root of the scan rate and the peak current (the slope is related to the relative electrochemically active surface area); (D) DRT analyses of TSC-200 and (E) DSC-200−0.3. (F) In situ XRD patterns during charge and discharge processes. (G) Geometric structure of single-atom defects. (H) Migration energy barrier of Li ions, the purple and black spheres in the crystal structure represent lithium and carbon atoms, respectively.

that the diffusion rate of lithium ions slows down with increasing lithiation. Notably, the lithium ion diffusion coefficient (D_{Li^+}) for DSC-200−0.3 is higher than that for TSC-200. This increased efficiency is attributed to the larger layer spacing in DSC-200−0.3, which reduces the energy barrier for lithium ion diffusion and thus enhances the reaction kinetics. Further cyclic voltammetry (CV) studies of TSC-200 and DSC-200−0.3 were carried out aiming at understanding their superior interfacial reaction kinetics. The CV profiles, captured at varying scan rates from 0.1 to 0.8 mV/s, are shown in Figure S18. Analysis based on the power law relationship between peak current and scan rate allows the determination of lithium-ion storage behavior by calculating the "*b*" value.[33] The slope values for TSC-200 and DSC-200−0.3 are 1.00 and 1.74, respectively (as depicted in Figure 5C). Thus, the dual-shock chemical strategy increases the relative active surface area in DSC-200−0.3 by almost 1.74 times compared to TSC-200, significantly enlarging the electrochemically active sites and enhancing interfacial reaction kinetics. As demonstrated in Figures S19 and S20. the log *i* and log *v* curve analyses show that the "*b*" values for the cathodic and anodic peaks of DSC-200−0.3 are 0.80 and 0.69, respectively. This suggests that the charging process predominantly involves pseudocapacitive ion storage behavior, while the discharge process remains diffusion-controlled. In contrast, TSC-200 exhibits the "*b*" values of 0.58 and 0.62 for its cathodic and anodic peaks, respectively, indicating that its charge−discharge (lithiation) process is primarily governed by a diffusion-controlled mechanism.

To enhance the understanding of the kinetics variation in TSC-200 and DSC-200−0.3 during different stage transitions, we applied in situ electrochemical impedance spectroscopy (EIS) methods. The resultant Nyquist diagrams, captured during the discharging process, are presented in Figure S21. These diagrams typically feature two incomplete semicircles, indicative of the solid electrolyte interface (SEI) layer

https://doi.org/10.1021/acsnano.4c02300
ACS Nano 2024, 18, 18344−18354

resistance (R_{SEI}) in the high-frequency domain and the charge transfer resistance (R_{ct}) in the low-frequency domain. To elucidate the substeps within the electrode process, distribution of relaxation time (DRT)[34,35] techniques are employed (Figure 5D,E). The peaks in the DRT analysis, alongside their corresponding kinetic processes, are detailed in Table S7.[36] Specifically, τ4 is related to the transfer of lithium ions to the electrode surface, while τ5 is dominated by the lithium-ion intercalation process.[37] It is noteworthy that the resistance values at τ4 and τ5 are considerably high (Table S8), indicating a deceleration of the charge transfer process. Consequently, the τ4 and τ5 steps are recognized as rate-determining steps in the lithiation process. The observed reduction in τ4 and τ5 resistance of DSC-200−0.3 further illustrates that double-shocked carbon can significantly expedite the kinetics of Li-ion intercalation, particularly in this crucial rate-determining step.

The in situ X-ray diffraction (XRD) charge−discharge test of the sample further elucidated both the storage mechanism and the structural stability of the lithium-ion battery as presented in Figure 5F. During lithiation, as the potential drops from the open circuit voltage to 0.01 V, there is a notable leftward shift of the (002) peak of the TSC-200 sample (Figure 5F−I), signifying that Li ions predominantly intercalate into the graphite layers. This peak returns to its original position upon recharging to 3.0 V. However, repeated charging and discharging cycles can cause structural damage, leading to a swift decline in capacity over prolonged cycles. In contrast, for the DSC-200−0.3 sample (Figure 5F−II), the displacement of the 002 peak is minimal. This suggests that Li ions are primarily stored within the larger interlayer spaces and adsorbed onto the surface of carbon layers, thereby preserving the carbon lattice structure. As a result, the hybrid-structured carbon anodes demonstrate exceptional cycle stability through multiple charging and discharging cycles.

To gain deeper insights into the mechanism through which the dual-shock chemical strategy enhances lithium-ion intercalation kinetics in the rate-determining step, density functional theory (DFT) calculations were conducted. Various models with different interlayer spacings commonly observed in graphite were constructed as shown in Figure 5G,H. The results indicate that as the interlayer spacing increases, the migration energy barriers for Li ions gradually decrease, from 1.18, 1.01, 0.82, and 0.63 eV. Amorphous carbon has a larger interlayer spacing and more lithium storage sites, which can facilitate the transport of lithium ions between the electrode material and the electrolyte. Good electrical conductivity of graphite contributes to the speedy charge transfer in lithium-ion batteries. The hybrid-structured carbon of the dual-shock chemistry strategy synthesis combines the advantages of both to achieve rapid transport of lithium ions.

CONCLUSIONS

In summary, the in situ dual-shock chemistry strategy has successfully prepared a carbon material for lithium-ion batteries, characterized by a combination of disordered and ordered structures. This approach involves leveraging ultrafast DSC chemistry to induce the ordering of carbon crystallites through thermal shock, while simultaneously ensuring structural disorder via mechanical thermal shock. Within this framework, disordered carbon serves as a proton transfer channel, effectively shortening the ion diffusion pathway. This amalgamated structure of ordered and disordered components yields an electrochemical performance of 208.61 mAh/g at a 10C rate, which is a substantial improvement over the 15 mAh/g performance of traditional graphite. Furthermore, after 3000 charge−discharge cycles, the material maintains a capacity retention rate of 81.06%. Advanced analytical techniques, including in situ XRD, DRT analysis, and DFT calculations, have elucidated that this exceptional rate performance is attributed to the expansive interlayer spacing (which facilitates ion transport) and the synergistic combination of graphite microcrystals with amorphous carbon (enhancing charge transfer). This research presents a pathway for accelerating the charging of lithium-ion batteries and holds potential for activating other carbon-based materials.

EXPERIMENTAL SECTION

Preparation of Materials. In a typical synthesis process, petroleum coke is mixed uniformly with Na_2CO_3 and NaCl using a ball mill. Subsequently, a certain mass of the mixed powder is accurately weighed and loaded into a quartz tube (inner diameter 6 mm, wall thickness 2 mm, length 100 mm), with graphite rods used to seal both ends of the sample. The graphite rod ends are connected to a capacitor bank (60mF), and the sample is subjected to discharge treatment at varying voltages, heating the sample to temperatures as high as 3000 K. After the equipment naturally cools to room temperature, the sample is extracted from the quartz tube, ground using a mortar and pestle, and then repeatedly washed with hydrochloric acid and deionized water. Finally, after drying under vacuum at 60 °C for 24 h, the prepared sample is obtained. For specific process parameters, please refer to Tables S1 and S2.

Material Characterization. The morphology and microstructure of TSC and DSC were studied by SEM (MAIA3 LMH) and a transmission electron microscope (TEM, JEOL JEM 2100F). X-ray powder diffraction (XRD) was conducted using a Bruker D-8 Advance diffractometer with nickel-filtered Cu-Kα (λ = 1.54178 Å) radiation at room temperature, and the data was collected from 5 to 80° with a scan rate of 2°/min to obtain the phase structure of TSC and DSC. Raman measurements were done for the composite by a Raman spectrometer (Senterra, Bruker, Germany) equipped with a 532 nm laser line to determine the chemical composition and structure of TSC and DSC. X-ray photoelectron spectroscopy (XPS) spectra were collected using a Thermal Scientific ESCALAB 250.

Electrochemical Characterization. All electrochemical tests were conducted within CR2032 cells, which were assembled inside a glovebox filled with high-purity argon (H_2O < 0.1 ppm, O_2 < 0.1 ppm). The working electrodes were composed of a mass ratio of 8:1:1 of active material, conductive carbon black, and poly(vinylidene fluoride) (PVDF). The active mass loading for each electrode was in the range of 1.5−2 mg/cm. The electrodes were fabricated using pure lithium foil as the current collector, Celgard 2400 polypropylene film as the separator, and a 1.0 M LiPF6 electrolyte solution in a 1:1 volume ratio of ethylene carbonate/diethyl carbonate (EC/DEC). Lithium-ion storage performance and Galvanostatic Intermittent Titration Technique (GITT) tests were recorded using a Newway battery testing system, with a voltage range of 0.01−3.00 V vs Li^+/Li. Cyclic voltammetry (CV) curves and impedance spectroscopy tests were measured at various scan rates using a CHI electrochemical workstation.

https://doi.org/10.1021/acsnano.4c02300
ACS Nano 2024, 18, 18344−18354

DFT Computational. In this work, we employed the Vienna Ab initio Simulation Package (VASP) along with the projector-augmented wave (PAW) method for our density functional theory (DFT) calculations.[38] For the exchange and correlation functional energy, we utilized the generalized gradient approximation (GGA) with the Perdew−Burke−Ernzerhof (PBE) functional.[39] The electronic wave functions were expanded in a plane-wave basis set, with a cutoff energy set to 520 eV to ensure convergence of the total energy. A plane-wave basis set with a cutoff energy of 520 eV and the Monkhorst−Pack mesh centered on γ were used to sample the Brillouin zone for integration, employing a k-point mesh resolution of $2\pi \times 0.03$ Å^{-1}.[40] For modeling the migration processes and identifying transition states and energy barriers, we used the climbing-image nudged elastic band (CI-NEB) method.[41] The convergence criterion for the force acting on the atoms during the CI-NEB calculations was set to less than 0.02 eV/Å. We also incorporated the DFT-D3 correction[42] to account for dispersion interactions, which are critical for accurate modeling of weakly bound structures. To further ensure the accuracy and reproducibility of our results, we tested the sensitivity of our findings to variations in the cutoff energy and k-point density.

Finite Element Simulation. The model structure is shown in Figure S3: the left and right are petroleum coke precursors, which are cylindrical particles with a height of 72 μm and a diameter of 72 μm; in the middle are Na_2CO_3 and NaCl, using different contact methods, surface, line, and point contact. The initial temperature of all materials is 293.15. The relevant properties of the materials are shown in Table S3.

ASSOCIATED CONTENT

Supporting Information

The Supporting Information is available free of charge at https://pubs.acs.org/doi/10.1021/acsnano.4c02300.

Schematic of equipment; Raman spectra; XRD; and other graphs and data (PDF)

AUTHOR INFORMATION

Corresponding Authors

Xinxi Zhang − *Key Laboratory of Coal Processing and Efficient Utilization of Ministry of Education, China University of Mining and Technology, Xuzhou 221116 Jiangsu, China*; Email: zhangxinxi@126.com

Rongtao Zhu − *Key Laboratory of Coal Processing and Efficient Utilization of Ministry of Education, China University of Mining and Technology, Xuzhou 221116 Jiangsu, China*; Email: rtzhu2010@cumt.edu.cn

Yanan Chen − *School of Materials Science and Engineering, Key Laboratory of Advanced Ceramics, Machining Technology of Ministry of Education, Tianjin Key Laboratory of Composite and Functional Materials, Tianjin University, Tianjin 300072, China*; orcid.org/0000-0002-6346-6372; Email: yananchen@tju.edu.cn

Authors

Pengfei Huang − *Key Laboratory of Coal Processing and Efficient Utilization of Ministry of Education, China University of Mining and Technology, Xuzhou 221116 Jiangsu, China; School of Materials Science and Engineering, Key Laboratory of Advanced Ceramics, Machining Technology of Ministry of Education, Tianjin Key Laboratory of Composite and Functional Materials, Tianjin University, Tianjin 300072, China*

Zekun Li − *School of Materials Science and Engineering, Key Laboratory of Advanced Ceramics, Machining Technology of Ministry of Education, Tianjin Key Laboratory of Composite and Functional Materials, Tianjin University, Tianjin 300072, China*

Li Chen − *School of Materials Science and Engineering, Key Laboratory of Advanced Ceramics, Machining Technology of Ministry of Education, Tianjin Key Laboratory of Composite and Functional Materials, Tianjin University, Tianjin 300072, China*

Yuan Li − *School of Materials Science and Engineering, Key Laboratory of Advanced Ceramics, Machining Technology of Ministry of Education, Tianjin Key Laboratory of Composite and Functional Materials, Tianjin University, Tianjin 300072, China*

Zhedong Liu − *School of Materials Science and Engineering, Key Laboratory of Advanced Ceramics, Machining Technology of Ministry of Education, Tianjin Key Laboratory of Composite and Functional Materials, Tianjin University, Tianjin 300072, China*

Jingchao Zhang − *School of Materials Science and Engineering, Key Laboratory of Advanced Ceramics, Machining Technology of Ministry of Education, Tianjin Key Laboratory of Composite and Functional Materials, Tianjin University, Tianjin 300072, China*

Jiawei Luo − *School of Materials Science and Engineering, Key Laboratory of Advanced Ceramics, Machining Technology of Ministry of Education, Tianjin Key Laboratory of Composite and Functional Materials, Tianjin University, Tianjin 300072, China*

Wenjun Zhang − *Key Laboratory of Coal Processing and Efficient Utilization of Ministry of Education, China University of Mining and Technology, Xuzhou 221116 Jiangsu, China*

Wei-Di Liu − *School of Chemistry and Physics, ARC Research Hub in Zero-emission Power Generation for Carbon Neutrality, and Centre for Materials Science, Queensland University of Technology, Brisbane 4000, Australia*; orcid.org/0000-0002-8271-639X

Complete contact information is available at: https://pubs.acs.org/10.1021/acsnano.4c02300

Author Contributions

Y.C.: planned and supervised the project. P.H.: conducted material synthesis, characterization, and analysis. P.H. and Z.L.: acquired and analyzed STEM data. P.H.: wrote the manuscript, and all authors contributed to the discussion and provided feedback on the manuscript.

Notes

The authors declare no competing financial interest.

ACKNOWLEDGMENTS

The authors acknowledge the financial support from the National Natural Science Foundation of China (Nos. 92372107, 52171219, and 51974307).

REFERENCES

(1) Armand, M.; Tarascon, J. M. Building better batteries. *Nature* **2008**, *451*, 652−657.

(2) Zhong, C.; Weng, S.; Wang, Z.; Zhan, C.; Wang, X. Kinetic limits and enhancement of graphite anode for fast-charging lithium-ion batteries. *Nano Energy* **2023**, *117*, No. 108894.
(3) Wang, C.-Y.; Liu, T.; Yang, X.-G.; Ge, S.; Stanley, N. V.; Rountree, E. S.; Leng, Y.; McCarthy, B. D. Fast charging of energy-dense lithium-ion batteries. *Nature* **2022**, *611*, 485−490.
(4) Fu, Y.; Jin, Y.; Ma, J.; Liu, J.; Wang, Z.; Wang, B.; Gong, X. Lithium-ion transfer strengthened by graphite tailings and coking coal for high-rate performance anode. *Chem. Eng. J.* **2022**, *442*, No. 136184.
(5) Chen, W.; Salvatierra, R. V.; Li, J. T.; Kittrell, C.; Beckham, J. L.; Wyss, K. M.; La, N.; Savas, P. E.; Ge, C.; Advincula, P. A.; et al. Flash Recycling of Graphite Anodes. *Adv. Mater.* **2023**, *35*, No. 2207303.
(6) Huang, Y.; Wang, C.; Lv, H.; Xie, Y.; Zhou, S.; Ye, Y.; Zhou, E.; Zhu, T.; Xie, H.; Jiang, W.; et al. Bifunctional Interphase Promotes Li + De-Solvation and Transportation Enabling Fast-Charging Graphite Anode at Low Temperature. *Adv. Mater.* **2023**, *36*, No. 2308675.
(7) Mu, Y.; Han, M.; Li, J.; Liang, J.; Yu, J. Growing vertical graphene sheets on natural graphite for fast charging lithium-ion batteries. *Carbon* **2021**, *173*, 477−484.
(8) Liu, T.; Zhang, R.; Zhang, X.; Liu, K.; Liu, Y.; Yan, P. One-step room-temperature preparation of expanded graphite. *Carbon* **2017**, *119*, 544−547.
(9) Meng, C.; Yuan, M.; Cao, B.; Jiang, Z.; Zhang, J.; Li, A.; Chen, X.; Jia, M.; Song, H. Insight into the structural evolution mechanism and potassium storage performance of expanded graphitic onion-like carbon. *J. Mater. Chem. A* **2022**, *10*, 22236−22244.
(10) Wang, R.; Yang, J.; Chen, X.; Zhao, Y.; Zhao, W.; Qian, G.; Li, S.; Xiao, Y.; Chen, H.; Ye, Y.; et al. Highly Dispersed Cobalt Clusters in Nitrogen-Doped Porous Carbon Enable Multiple Effects for High-Performance Li−S Battery. *Adv. Energy Mater.* **2020**, *10*, No. 1903550.
(11) Kim, J.; Shin, M.; So, S. H.; Hong, S.; Park, D. Y.; Kim, C.; Park, C. R. Correlation between structural characteristics of edge selectively-oxidized graphite and electrochemical performances under fast charging condition. *Carbon* **2024**, *218*, No. 118664.
(12) Chen, K.-H.; Goel, V.; Namkoong, M. J.; Wied, M.; Müller, S.; Wood, V.; Sakamoto, J.; Thornton, K.; Dasgupta, N. P. Enabling 6C Fast Charging of Li-Ion Batteries with Graphite/Hard Carbon Hybrid Anodes. *Adv. Energy Mater.* **2021**, *11*, No. 2003336.
(13) Yang, X.-G.; Liu, T.; Gao, Y.; Ge, S.; Leng, Y.; Wang, D.; Wang, C.-Y. Asymmetric Temperature Modulation for Extreme Fast Charging of Lithium-Ion Batteries. *Joule* **2019**, *3*, 3002−3019.
(14) An, J.; Wang, F.; Yang, J.-Y.; Li, G.; Li, Y. An Ion-Pumping Interphase on Graphdiyne/Graphite Heterojunction for Fast-Charging Lithium-Ion Batteries. *CCS Chem.* **2024**, *6*, 110−124.
(15) Wang, L.; Du, C.; Li, Z.; Han, Y.; Feng, N.; Yang, J. Catalytic graphitization of coke and electrochemical performances of coke-based graphite. *J. Alloys Compd.* **2023**, *960*, No. 170949.
(16) Li, L.; Zhang, D.; Deng, J.; Gou, Y.; Fang, J.; Cui, H.; Zhao, Y.; Cao, M. Carbon-based materials for fast charging lithium-ion batteries. *Carbon* **2021**, *183*, 721−734.
(17) Luong, D. X.; Bets, K. V.; Algozeeb, W. A.; Stanford, M. G.; Kittrell, C.; Chen, W.; Salvatierra, R. V.; Ren, M.; McHugh, E. A.; Advincula, P. A.; et al. Gram-scale bottom-up flash graphene synthesis. *Nature* **2020**, *577*, 647−651.
(18) Dou, S.; Xu, J.; Cui, X.; Liu, W.; Zhang, Z.; Deng, Y.; Hu, W.; Chen, Y. High-Temperature Shock Enabled Nanomanufacturing for Energy-Related Applications. *Adv. Energy Mater.* **2020**, *10*, No. 2001331.
(19) Yang, W.; Zhou, J.; Wang, S.; Wang, Z.; Lv, F.; Zhang, W.; Zhang, W.; Sun, Q.; Guo, S. A three-dimensional carbon framework constructed by N/S co-doped graphene nanosheets with expanded interlayer spacing facilitates potassium ion storage. *ACS Energy Lett.* **2020**, *5*, 1653−1661.
(20) Gao, L. T.; Huang, P.; Guo, Z.-S. Understanding Charge-Transfer and Mass-Transfer Effects on Dendrite Growth and Fast Charging of Li Metal Battery. *J. Electrochem. Soc.* **2023**, *170*, No. 050512.
(21) Xu, B.; Cao, Q.; Kuang, D.; Gasem, K. A.; Adidharma, H.; Ding, D.; Fan, M. Kinetics and mechanism of CO_2 gasification of coal catalyzed by Na_2CO_3, $FeCO_3$ and Na_2CO_3−$FeCO_3$. *J. Energy Inst.* **2020**, *93*, 922−933.
(22) Yuan, L.; Liu, Q.; Mathews, J. P.; Zhang, H.; Wu, Y. Quantifying the Structural Transitions of Chinese Coal to Coal-Derived Natural Graphite by XRD, Raman Spectroscopy, and HRTEM Image Analyses. *Energy Fuels* **2021**, *35*, 2335−2346.
(23) Hallam, K. R.; Darnbrough, J. E.; Paraskevoulakos, C.; Heard, P. J.; Marrow, T. J.; Flewitt, P. E. J. Measurements by x-ray diffraction of the temperature dependence of lattice parameter and crystallite size for isostatically-pressed graphite. *Carbon Trends* **2021**, *4*, No. 100071.
(24) Khalfaoui, M.; Knani, S.; Hachicha, M. A.; Lamine, A. B. New theoretical expressions for the five adsorption type isotherms classified by BET based on statistical physics treatment. *J. Colloid Interface Sci.* **2003**, *263*, 350−356.
(25) Cheng, Q.; Yuge, R.; Nakahara, K.; Tamura, N.; Miyamoto, S. KOH etched graphite for fast chargeable lithium-ion batteries. *J. Power Sources.* **2015**, *284*, 258−263.
(26) Shim, J.-H.; Lee, S. Characterization of graphite etched with potassium hydroxide and its application in fast-rechargeable lithium ion batteries. *J. Power Sources* **2016**, *324*, 475−483.
(27) Kim, J.; Jeghan, S. M. N.; Lee, G. Superior fast-charging capability of graphite anode via facile surface treatment for lithium-ion batteries. *Microporous Mesoporous Mater.* **2020**, *305*, No. 110325.
(28) Son, D.-K.; Kim, J.; Raj, M. R.; Lee, G. Elucidating the structural redox behaviors of nanostructured expanded graphite anodes toward fast-charging and high-performance lithium-ion batteries. *Carbon* **2021**, *175*, 187−201.
(29) Billaud, J.; Bouville, F.; Magrini, T.; Villevieille, C.; Studart, A. R. Magnetically aligned graphite electrodes for high-rate performance Li-ion batteries. *Nat. Energy* **2016**, *1*, No. 16097.
(30) Lee, S.-M.; Kim, J.; Moon, J.; Jung, K.-N.; Kim, J. H.; Park, G.-J.; Choi, J.-H.; Rhee, D. Y.; Kim, J.-S.; Lee, J.-W.; Park, M.-S. A cooperative biphasic MoOx−MoPx promoter enables a fast-charging lithium-ion battery. *Nat. Commun.* **2021**, *12*, No. 39.
(31) Xu, C.; Ma, G.; Yang, W.; Che, S.; Li, Y.; Jia, Y.; Liu, H.; Chen, F.; Zhang, G.; Liu, H.; et al. One-step reconstruction of acid treated spent graphite for high capacity and fast charging lithium-ion batteries. *Electrochim. Acta* **2022**, *415*, No. 140198.
(32) Holtstiege, F.; Koç, T.; Hundehege, T.; Siozios, V.; Winter, M.; Placke, T. Toward High Power Batteries: Pre-lithiated Carbon Nanospheres as High Rate Anode Material for Lithium Ion Batteries. *ACS Appl. Energy Mater.* **2018**, *1*, 4321−4331.
(33) He, H.; He, J.; Yu, H.; Zeng, L.; Luo, D.; Zhang, C. Dual-Interfering Chemistry for Soft-Hard Carbon Translation toward Fast and Durable Sodium Storage. *Adv. Energy Mater.* **2023**, *13*, No. 2300357.
(34) Ciucci, F. The Gaussian Process Hilbert Transform (GP-HT): Testing the Consistency of Electrochemical Impedance Spectroscopy Data. *J. Electrochem. Soc.* **2020**, *167*, No. 126503.
(35) Liu, J.; Wan, T. H.; Ciucci, F. A Bayesian view on the Hilbert transform and the Kramers-Kronig transform of electrochemical impedance data: Probabilistic estimates and quality scores. *Electrochim. Acta* **2020**, *357*, No. 136864.
(36) Chen, J.; Quattrocchi, E.; Ciucci, F.; Chen, Y. Charging processes in lithium-oxygen batteries unraveled through the lens of the distribution of relaxation times. *Chem* **2023**, *9*, 2267−2281.
(37) Chen, X.; Li, L.; Liu, M.; Huang, T.; Yu, A. Detection of lithium plating in lithium-ion batteries by distribution of relaxation times. *J. Power Sources* **2021**, *496*, No. 229867.
(38) Kresse, G.; Furthmüller, J. Efficient iterative schemes for ab initio total-energy calculations using a plane-wave basis set. *Phys. Rev. B* **1996**, *54*, No. 11169.
(39) Kresse, G.; Joubert, D. From ultrasoft pseudopotentials to the projector augmented-wave method. *Phys. Rev. B* **1999**, *59*, 1758−1775.
(40) Monkhorst, H. J.; Pack, J. D. Special points for Brillouin-zone integrations. *Phys. Rev. B* **1976**, *13*, 5188−5192.

https://doi.org/10.1021/acsnano.4c02300
ACS Nano 2024, 18, 18344−18354

(41) Henkelman, G.; Uberuaga, B. P.; Jónsson, H. A climbing image nudged elastic band method for finding saddle points and minimum energy paths. *J. Chem. Phys.* **2000**, *113*, 9901−9904.
(42) Moellmann, J.; Grimme, S. DFT-D3 Study of Some Molecular Crystals. *J. Phys. Chem. C* **2014**, *118*, 7615−7621.

https://doi.org/10.1021/acsnano.4c02300
ACS Nano 2024, 18, 18344−18354